

# Removal of Zn(II) By Magnetic Composite Adsorbent: Synthesis, Performance, And Mechanism

Shuang Yi (✉ [597049335@qq.com](mailto:597049335@qq.com))

Guangdong University of Technology <https://orcid.org/0000-0001-9450-1823>

Binqin Bao

Guangdong University of Technology

Weifeng Song

Guangdong University of Technology

MuDdan Liu

Guangdong Academy of Sciences

---

## Research Article

**Keywords:** Adsorbent, L-methionine, Efficient Zn(II) removal, Magnetic gel sphere, Mechanism

**Posted Date:** December 20th, 2021

**DOI:** <https://doi.org/10.21203/rs.3.rs-1113178/v1>

**License:**  This work is licensed under a Creative Commons Attribution 4.0 International License.

[Read Full License](#)

---

**Version of Record:** A version of this preprint was published at Environmental Science and Pollution Research on March 31st, 2022. See the published version at <https://doi.org/10.1007/s11356-022-19830-7>.

# Abstract

In this study, L-methionine and nano-Fe<sub>3</sub>O<sub>4</sub> were encapsulated and cured on sodium alginate by the ionic cross-linking method to form magnetic composite gel spheres (SML). The influence of adsorbent dosages, pH, reaction time, and initial ion concentration on the ability of the gel spheres to adsorb Zn(II) was investigated. The experimental results indicated that under the optimum conditions, the maximum amount of Zn(II) adsorbed by the adsorbent gel spheres reached 86.84 mg·g<sup>-1</sup>. The experimental results of adsorption indicate that the reaction process of this adsorbent fits well with the Langmuir and pseudo-second-order kinetic models and is a heat absorption reaction. The results of the adsorption investigation of the coexistence system showed that the adsorbent would preferentially adsorb Pb(II), and the adsorption efficiency of Zn(II) decreased when the concentration of interfering ions increased. The structure of this adsorbent and the adsorption mechanism were investigated by Fourier transform infrared spectrometer, thermal gravimetric analyzer, vibrating sample magnetometer, scanning electron microscope, Brunner-Emmet-Teller measurements, and X-ray photoelectron spectroscopy. The results show that this magnetic composite adsorbent is a mesoporous material with superior adsorption performance, and the amino and carboxyl groups on it react with Zn(II) via ligand chelation; the ion exchange effect of Ca(II) also plays a role. The desorption-adsorption experiments of the adsorbent indicated that the adsorption amount of Zn(II) was maintained at a higher level after several cycles, and the loss of Fe was approximately 0.2%. In summary, SML is an ideal adsorbent for environmental protection.

## Introduction

Water is a vital resource for human survival. With the rapid growth of industrialization and urbanization, hazardous industrial waste is discharged into the environment through wastewater, causing tremendous damage to the ecological environment. Most heavy metals cannot be biodegraded and accumulate in the environment, which deteriorates the quality of water and causes incurable damage to human health (Huang et al. 2018; Thasneema et al. 2021; Wang et al. 2016).

Zinc is mostly used in the electroplating, paint and coating, textile, chemical, and paper industries and generates a large amount of zinc-containing wastewater (Hoseinian et al. 2017). Zinc is difficult to degrade in water and accumulates in water (Liu et al. 2020). Zinc is an essential element of the human body and regulates many physiological activities. However, excessive amounts of zinc can harm human health, causing diseases such as anemia (Fu & Wang, 2011). Consequently, the treatment of zinc-containing wastewater remains a major research topic in the field of environmental protection.

Processes, namely chemical precipitation, photocatalysis, electrodeposition, photocatalysis, and sorption (Fang et al. 2018; Godiya et al. 2019; Mao et al. 2021), have been widely used in the advanced treatment of wastewater containing Zn(II). Among several processes, adsorption is considered the most efficient method for the treatment of heavy metals because of its simplicity of operation, excellent adsorption performance, cost-effectiveness, and selectivity for heavy metal ions based on synthetic raw materials

(Godiya et al. 2019; Chai et al. 2021; Jin et al. 2019; Varghese et al. 2019). Many related studies have been on traditional adsorbent types, including activated carbon (Skubiszewska-Zieba et al. 2017), ion exchange materials (Fu et al. 2018), zeolites (Garg et al. 2015), clay mineral materials (Soltani et al. 2019), biosorbents such as cellulose (Deghles et al. 2019), chitosan (Zhang et al. 2020), and fruit waste (Gopalakrishnan et al. 2020). However, most traditional adsorbents are costly, and biosorbents are modified or cross-linked by hazardous chemicals to improve their adsorption ability, which means they are unfriendly to the environment. For instance, to improve the adsorption capacity, phthalic anhydride was employed to modify chitosan (Ghiggi et al. 2017). In the case of cellulose, triethylenetetramine is considered an effective material for increasing adsorption capacity (Gurgel & Gil 2009). Hence, preparing a highly efficient adsorbent that has outstanding recyclability and is environmentally friendly is important.

Sodium alginate (SA) is a natural polysaccharide carbohydrate with excellent characteristics such as high biocompatibility, biodegradability, and regeneration (Gurgel & Gil 2009). SA, as a large molecule adsorbent, has a molecular chain rich in hydroxyl and carboxyl groups, which are available for heavy metal ions adsorption and other reactions to form hydrogels; can maintain a good swelling state in water but is insoluble in water; and is available for a wide range of wastewater treatment applications (Wang et al. 2019). Polyfunctional groups can also be used for cross-linking. However, the adsorption capacity of a single SA is limited because of the insufficient adsorption sites; thus, it needs to be modified to improve its adsorption capacity. Mousa et al. (2016) prepared hydrogel spheres by combining montmorillonite with SA by cross-linking with calcium chloride, and the adsorption amount of  $Pb^{2+}$  reached  $244.6 \text{ mg}\cdot\text{g}^{-1}$ . He et al. (2019) used SA encapsulated carboxymethyl chitosan and kaolin clay to produce a new gel sphere with an adsorption capacity of  $Cu^{2+}$  up to  $206 \text{ mg}\cdot\text{g}^{-1}$ . The findings of these studies revealed that the removal capacity of SA hydrogels for metals was significantly improved by modification. In this regard, the selection of modifiers is particularly important for the improvement of SA adsorption performance. Methionine (L-met), an essential amino acid, has carboxyl and amino groups, which are easily complexed with divalent metal ions in solution, and the introduction of these groups will substantially enhance the adsorption capacity of SA. Because of its nontoxicity and good biocompatibility, it has the potential to become a promising environmental modifier (Giles et al. 2003; Kumar et al. 2013). However, if the adsorbent cannot be recycled, its acquisition is a waste of resources, and there remains a risk of environmental contamination.  $Fe_3O_4$  nanoparticles have received wide interest for their excellent magnetic response properties and low biotoxicity.  $Fe_3O_4$  nanoparticles show good response performance even at low magnetic field strengths (Yavuz et al. 2006), and the loading on the adsorbent can result in a fast recycling function. Additionally,  $Fe_3O_4$  nanoparticles can enhance heavy metal adsorption performance (Song et al. 2018). Moreover, magnetic SA is prepared by an embedding method without the use of hazardous substances such as potent oxidizing agents or other chemicals.

Consequently, this work proposes using methionine to modify SA hydrogel and introduce a magnetic medium to make it magnetically responsive to obtain SML, which has high adsorption ability and rapid recycling. SML was characterized using a scanning electron microscope (SEM), Fourier transform

infrared spectrometer (FTIR), thermal gravimetric analyzer (TGA), and vibrating sample magnetometer (VSM). Its structural features and reaction mechanisms were investigated using Brunner-Emmet-Teller measurements (BET) and X-ray photoelectron spectroscopy (XPS). The effects of the initial pH of the reaction system, SML dosage, reaction time, and initial concentration of metal ions were investigated, and the cyclic performance of the SML was also investigated.

## Materials And Methods

### Materials

SA, methionine, and calcium chloride ( $\text{CaCl}_2$ ) were obtained from Aladdin Reagent Co., Ltd. (Shanghai, China). Ferric chloride hexahydrate ( $\text{FeCl}_3 \cdot 6\text{H}_2\text{O}$ ), ferrous chloride tetrahydrate ( $\text{FeCl}_2 \cdot 4\text{H}_2\text{O}$ ), and ammonia monohydrate ( $\text{NH}_3 \cdot \text{H}_2\text{O}$ ) were acquired from Damao Chemical Reagent Factory (Tianjin, China). Zinc nitrate ( $\text{Zn}(\text{NO}_3)_2$ ), hydrochloric acid (HCl), nitric acid ( $\text{HNO}_3$ ), and sodium hydroxide (NaOH) were acquired from Guangzhou Chemical Reagent Factory Co., Ltd. (Guangzhou, China).

### SML Preparation

First, nanoscale  $\text{Fe}_3\text{O}_4$  particles were prepared. First, 100 mL ultrapure water was mixed with  $\text{FeCl}_3 \cdot 6\text{H}_2\text{O}$  and  $\text{FeCl}_2 \cdot 4\text{H}_2\text{O}$  in a molar ratio of 2:1, and reacted at  $85^\circ\text{C}$  in  $\text{N}_2$  atmosphere 1 h.  $\text{NH}_3 \cdot \text{H}_2\text{O}$  solution was added to the flask, making the pH reach 10 and then react at  $80^\circ\text{C}$  for 2 h under constant conditions, and a magnet was used to separate the synthesized  $\text{Fe}_3\text{O}_4$  nanoparticles. The samples were washed several times with ethanol and ultrapure water and dried at  $60^\circ\text{C}$ . These steps represent the preparation of SML.  $\text{Fe}_3\text{O}_4$  nanoparticles were ultrasonically distributed in 100 mL of water for 5 min. SA (3 g) and methionine (0.5 g) were added to the aforementioned solution and mixed at  $200 \text{ r} \cdot \text{min}^{-1}$  for 3 h. The product was added to a  $\text{CaCl}_2$  solution at a rate of 1 drop per second, cured for 8 h, filtered and washed a few times, and dried at  $60^\circ\text{C}$  to obtain the final product.

### Characterization

Surface functional groups of the adsorbents were obtained using Fourier transform infrared spectrometer (FTIR, Tensor 27, Bruker, Germany). Changes in the adsorbents from 2 to  $900^\circ\text{C}$  were observed using a TGA, PerkinElmer, USA) at a heating rate of  $5^\circ\text{C}/\text{min}$ . The magnetic performance of the samples was characterized using a VSM (7400, Lake Shore, USA). The surface appearance of the adsorbents was observed using an SEM (650, USA). The relative surface area and pore diameter of the adsorbent were investigated using BET analysis (ASAP2460, Micromeritics Instrument, USA). The surface chemistry of the adsorbents was characterized using XPS (Thermo Fisher Scientific, USA).

### Adsorption experiments

Adsorption experiments were system pH (2-6), initial concentration of heavy metals ( $0\text{-}500 \text{ mg} \cdot \text{L}^{-1}$ ), reaction time (0–180 min), and dosage amount ( $0.1\text{-}2 \text{ g} \cdot \text{L}^{-1}$ ). In the experiment, system pH was

regulated with 0.1–0.5M HCl and NaOH. At the end of the adsorption process, the adsorbent was separated from the solution. Concentrations of the remaining metals in the supernatant were detected using flame atomic adsorption spectrometry. All adsorption studies were repeated twice, and the final average was used as the result. The adsorption capacity of SML and removal efficiency were calculated using Eqs. (1) and (2)(Yahaya et al. 2009).

$$q_e = \frac{(C_0 - C_e) V}{m}$$

1

$$Q_R = \frac{(C_0 - C_e)}{C_0} \times 100\%$$

2

$q_e$  ( $\text{mg}\cdot\text{g}^{-1}$ ) is the adsorption capacity of SML,  $Q_R$  is the removal efficiency of Zn(II),  $C_0$  ( $\text{mg}\cdot\text{L}^{-1}$ ) is the initial concentration of heavy metals in the solution,  $C_e$  ( $\text{mg}\cdot\text{L}^{-1}$ ) is the concentration of the residual metal in the solution,  $m$  (g) is the dosing amount, and  $V$  (L) is the solution volume.

## Desorption and regeneration

When the adsorption process was complete, magnetic gel spheres with Zn(II) adsorption were placed in 0.1  $\text{mol}\cdot\text{L}^{-1}$   $\text{HNO}_3$  solution, mechanically stirred for 30 min, and cleaned a few times with ultrapure water; gel spheres were then placed in a 2.5%  $\text{CaCl}_2$  solution, re-cured for 12 h, and washed and placed in a drying oven at 60°C.

## Results And Discussion

### Characterization

#### SEM analysis

The surface morphology of the magnetic composite gel spheres was dense and slightly rough, as shown in Fig. 1(a), which facilitates contact with Zn(II), mainly due to the cross-linking of the carboxyl group on SA with  $\text{Ca}^{2+}$  in the solution. As shown in Fig. 1(b), the internal mesh structure of SML with more folds provides a channel for Zn(II) to enter the gel sphere and expand the contact area between the target ions and adsorption sites. Figs. 1(c) and 1(d) show that Fe and N were evenly distributed on the surface, indicating that  $\text{Fe}_3\text{O}_4$  and L-met were uniformly distributed on the adsorbent.

#### FTIR analysis

The structure of the SML is shown in Fig. 2(a). The vibrational peak at  $3430\text{ cm}^{-1}$  is caused by the stretching of the -OH group vibration (Lin et al. 2012), indicating the presence of water crystallization in the magnetic composite gel spheres. The C-H group adsorption peak was observed at  $2930\text{ cm}^{-1}$ . The vibration bands at  $1421\text{ cm}^{-1}$  and  $1510\text{ cm}^{-1}$  represent the bending vibration peaks of the -COO and N-H bonds, respectively, indicating the presence of L-methionine in the composite material. The stretching bond, appearing near  $580\text{ cm}^{-1}$ , belongs to the peak of Fe-O, and it shows that  $\text{Fe}_3\text{O}_4$  loaded successfully in the composite material (Jiang et al. 2013).

### Thermogravimetric analysis

As shown in Fig. 2(b), the entire pyrolysis process of SML exhibited four weightlessness stages, and peaks appeared at 190, 290, 520, and  $750^\circ\text{C}$ . First, the weightlessness stages observed from room temperature to  $190^\circ\text{C}$  were mainly due to the reduction of free water, and the corresponding percentage of weightlessness was approximately 15.96%. Second, the relative weight loss of the magnetic adsorbent was approximately 29.45% for temperatures ranging from 190 to  $290^\circ\text{C}$ , which is related to the skeleton breakage of calcium alginate and the removal of the adjacent hydroxyl groups. Next, decomposition and carbonization of some carboxyl functional groups from 290 to  $500^\circ\text{C}$  caused a weight loss of approximately 11.15%. Finally, near 11.45% of weightlessness occurs under 520 to  $750^\circ\text{C}$ , which indicates further oxidation and decomposition of calcium alginate.

### Magnetic property analysis

Hysteresis lines of  $\text{Fe}_3\text{O}_4$  and SML were measured using a magnetometer to determine whether the resulting magnetic composite gel spheres could be separated quickly from water under an applied magnetic field.

In Fig. 2(c), both samples appear superparamagnetic and do not show hysteresis; the saturation magnetizations of SML and  $\text{Fe}_3\text{O}_4$  are  $72.92\text{ emu}\cdot\text{g}^{-1}$  and  $4.84\text{ emu}\cdot\text{g}^{-1}$ , respectively. Although the surface of the material is covered by SA, which degrades the magnet response performance, it maintains good performance and does not affect the magnetic separation effect. Under the condition of an applied magnetic field (0.4 T), a solid-liquid can be separated rapidly, facilitating recycling after adsorption and reducing the risk of secondary contamination.

## Adsorption

### Effect of pH on the adsorption of Zn(II)

Figure 3(a) shows the effect of pH on the adsorption ability of SML in simulated wastewater. In the beginning, the adsorption capacity increases as the pH increases; at  $\text{pH}=5$ , maximum adsorption ability is  $89.9\text{ mg}\cdot\text{g}^{-1}$ ; when  $\text{pH}=2$ , the adsorption effect of the adsorbent is poor. This is because the competitive adsorption between  $\text{H}^+$  and  $\text{Zn}^{2+}$  causes the carboxyl group, and the reduction of amino groups seriously affects the effect of SML. Because the functional group is protonated, the effect of electrostatic repulsion

is increased, which interferes with Zn(II) adsorption. As pH increases,  $H^+$  decreases to a large extent, the amino and carboxyl groups are rapidly deprotonated, and the electrostatic repulsion is gradually reduced, which increases the adsorption capacity of the gel spheres. When pH=6, the solution produced white precipitate  $Zn(OH)_2$ , which is not conducive to adsorption with the gel ball; therefore, the adsorption capacity decreased.

#### Effect of SML dosage on the adsorption of Zn(II)

Figure 3(b) presents the effects of SML dosage on target metal ion adsorption capacity. In this section, the removal rate increased as the SML dosage increased. The removal rate was nearly 70% when the dosage was  $0.7 \text{ g}\cdot\text{L}^{-1}$ , and the adsorption capacity remained at a high level with a slight decrease. A reasonable conclusion is that increasing the gel ball improved the adsorption properties and contact area with heavy metal ions. When the dosage of magnetic adsorbent reached  $2 \text{ g}\cdot\text{L}^{-1}$ , the removal efficiency was 90.14%, and the removal rate increased, whereas the adsorption capacity decreased. This finding can be explained as follows: excess adsorption sites on the gel ball lead to a decrease in the unit adsorption capacity. Thus,  $0.7 \text{ g}\cdot\text{L}^{-1}$  is the optimal dosage of SML based on the adsorption capacity and removal rate.

#### Effects of initial concentration on adsorption of Zn(II) on different materials

The adsorption performance improved with the increase in the initial concentration of Zn(II), as shown in Fig. 3(c), because the electrostatic gravitational force also gradually increases, and the adsorption sites of the gel spheres are easily occupied (Hongyu et al. 2015). The increase in adsorption gradually decreased at  $200 \text{ mg}\cdot\text{L}^{-1}$  to  $500 \text{ mg}\cdot\text{L}^{-1}$  and tended to reach equilibrium. Moreover, adsorption with gel spheres on metal ions encapsulated with L-met at initial concentrations of  $20 \text{ mg}\cdot\text{L}^{-1}$  to  $500 \text{ mg}\cdot\text{L}^{-1}$  is significantly higher than that of SA and SA@Fe<sub>3</sub>O<sub>4</sub>. This result demonstrates that the loading of L-met increases the effective functional groups of the gel spheres for heavy metal adsorption, which increases the quantity of adsorption spots of the material, improving the adsorption efficiency. The reason for the greater adsorption of SA than SA@Fe<sub>3</sub>O<sub>4</sub> is that the nanoscale Fe<sub>3</sub>O<sub>4</sub> in the gel spheres limits the contact of metal ions in solution with the sites, reducing the adsorption capacity of the material (Zhang et al. 2013).

#### Effect of time on adsorption of Zn(II) by SML at various starting concentrations

As shown in Fig. 3(d), the effect of SML on Zn(II) exhibited a rapid increase with the increase of adsorption time over 30 min. The leading cause of this situation is that the gel sphere has sufficient adsorption sites occupied by heavy metal ions, and there is a large concentration difference between the inside and outside of the gel sphere during the early period of adsorption. Metal ions diffuse rapidly to the surface of the gel sphere; some target heavy metals enter the gel sphere through ion exchange; and the higher the concentration gradient of the solution, the greater the driver will be at the beginning. Thus, the greater the original concentration of the metal, the faster the adsorption rate of the material. The amount

of Zn(II) adsorbed by SML reached 302.12 mg·L<sup>-1</sup> at 60 min, close to the adsorption equilibrium amount. After 60 min, the adsorption sites of Zn(II) gradually saturated, and the concentration difference between the heavy metal inside and outside the adsorbent decreased, which reduced the adsorption driver and led to gradual degradation in the adsorption rate. Additionally, the number of available adsorption sites on the material also slowly decreased, and this did not facilitate the adsorption process; thus, the adsorption capacity increased slowly and tended to dynamic equilibrium.

#### Adsorption kinetics analysis

Saturated adsorption of SML was 29.82, 51.2, 83.92, 86.84 mg·L<sup>-1</sup> at 20 to 200 mg·L<sup>-1</sup>, respectively.

Table.1 Calculated kinetic parameters for adsorption of Zn(II) by SML

Co(mg·L <sup>-1</sup> )	Pseudo-first-order kinetic model			Pseudo-second-order kinetic model		
	Q <sub>e</sub> (mg·g <sup>-1</sup> )	k <sub>1</sub>	R <sub>2</sub>	Q <sub>e</sub> (mg·g <sup>-1</sup> )	k <sub>2</sub>	R <sub>2</sub>
20	47.74	0.0895	0.9782	42.70	0.00348	0.993
50	95.12	0.0411	0.9753	94.61	0.00281	0.999
100	161.9	0.0237	0.9152	164.9	0.00194	0.999
200	323.1	0.0229	0.9223	328.8	0.00129	0.999

As shown in Table 1, the higher value of the regression coefficient for the pseudo-second-order model than that of the other models confirms this finding. The kinetics of Zn(II) adsorption by SML were governed by chemisorption.

#### Adsorption isotherms analysis

Table.2 Relevance parameters of SML for Zn(II) adsorption

Temp(°C)	Langmuir			Freundlich			
	Q <sub>max</sub> (mg·g <sup>-1</sup> )	k <sub>L</sub> (L·mg <sup>-1</sup> )	R <sup>2</sup>	R <sub>L</sub>	k <sub>L</sub> (L·mg <sup>-1</sup> )	n	R <sup>2</sup>
25	85.13	0.0618	0.995	0.0512	16.974	3.029	0.764
35	90.83	0.0671	0.997	0.0472	19.221	3.210	0.785
45	93.15	0.0762	0.997	0.0419	20.921	3.331	0.789
55	96.01	0.0761	0.997	0.0420	21.217	3.165	0.836

The results in Table 2 indicate that the reaction process of SML shows a relatively higher correlation in the Langmuir adsorption isotherm equation than in the Freundlich adsorption isotherm equation. The coefficients of determination R<sup>2</sup> were all greater than 0.99, indicating that the monomolecular layer of

SML after adsorption formed uniformly adsorbed onto the surface material. The separation constant at different temperatures was in the range of  $0 < RL < 1$ , indicating that the reaction process can proceed easily.  $K_f$  in the Freundlich model increased gradually from 25 to 55 °C, indicating that the increase in temperature can promote the adsorption reaction.

### Adsorption thermodynamic analysis

Table.3 Fitting parameters for adsorption thermodynamics of Zn(II) by the SML

Temp(°C)	$k_F$	$\Delta G/(\text{kJ}\cdot\text{mol}^{-1})$	$\Delta H(\text{kJ}\cdot\text{mol}^{-1})$	$\Delta S/(\text{J}\cdot\text{mol}^{-1})$
25	115.329	-11.762		55.804
35	121.857	-12.299	4.8667	55.732
45	129.423	-12.857		55.702
55	138.027	-13.437		55.654

Table 3 shows that  $\Delta G$  is -7.019,-7.573,-8.043, and -8.334  $\text{kJ}\cdot\text{mol}^{-1}$  at 25–55 °C, indicating that the gel sphere adsorption process is spontaneous. The entropy characteristics ( $\Delta S$ ) listed in Table 3 indicate that the adsorption reaction is a process of entropy increase. The enthalpy change( $\Delta H$ ) is 4.866  $\text{kJ}\cdot\text{mol}^{-1}$ , indicating that the sorption of Zn(II) belongs to the heat absorption process.

### Cycle performance

Figure 4 shows the cycle performance of the magnetic composite gel spheres. In this section, SML was used to conduct five adsorption-desorption experiments in  $0.1 \text{ mol}\cdot\text{L}^{-1} \text{ HNO}_3$ .

As shown in Fig. 4, some of the adsorption sites occupied by  $\text{H}^+$  are released and exposed again, and the adsorption capacity of the magnetic adsorbent on Zn(II) reaches  $58.65 \text{ mg}\cdot\text{g}^{-1}$  after five adsorption-desorption experiments. The concentration of Fe in the experiment's solution is  $0.24 \pm 0.02 \text{ mg}\cdot\text{L}^{-1}$ , and the leaching rate is 0.0629%. This phenomenon indicates that SML can still maintain good adsorption capacity after times adsorption-desorption experiments, with a low waste rate of Fe. Additionally, the stability of SML does not cause the threat of the instant release of heavy metals.

## Effect of coexisting ions

Effect of increasing total amount of Pb(II) on adsorption of material to Zn(II)

Zn(II) concentration in the solution system was limited to  $50 \text{ mg}\cdot\text{L}^{-1}$ ; the changes in sorption of two heavy metals by SML were investigated by increasing the concentration of Pb(II); and the Zn(II):Pb(II) concentration ratios were set to four concentration ratio gradients: 50:10, 50:25, 50:50, and 50:100.

As shown in Fig. 5(a), the adsorption of Pb(II) showed an increasing trend when the Pb(II) concentration in the solution system gradually increased from 10 to 100 mg. The adsorption amount of Zn(II) decreased from 30.26 to 18.73 mg, which indicated that interfering Pb(II) influenced the adsorption of magnetic composite gel spheres on Zn(II), and SML has preferential adsorption on Pb(II).

Effect of increasing total amount of Pb(II) on adsorption of material to Pb(II)

The concentration of Pb(II) was limited, and the variation of SML on Pb(II) adsorption was investigated by increasing the concentration of Zn(II) in the system. As shown in Fig. 5b, when the interfering ion concentration was increased from 10 to 100 mg, there was no influence on the sorption of Pb(II) by SML, and the amount of Pb(II) sorption remained at approximately 50 mg. As the concentration of exogenous ion Pb(II) increased, although the amounts of Zn(II) adsorbed steadily increased to 37.81 mg, they were still much lower than those of Pb(II) adsorption. This difference might be mainly because the ionic radius of Pb(II) is 119 pm, which is greater than that of Zn(II) (83 pm); therefore, the polarization force is smaller for Pb(II) ions than for Zn(II), which facilitates complexation with functional groups and thus preferential adsorption on Pb(II). Zhu et al.(2012) prepared modified chitosan magnetic gel spheres and found that the order of competing order was Pb(II) > Zn(II), and our experimental findings are in agreement with this conclusion.

## Adsorption mechanism

BET analysis

The results of the pore size distribution and adsorption-desorption isotherms are presented in Figure 6. Fig. 6(a) shows that the relative surface area of the SML is 10.11 m<sup>2</sup>/g, average pore size is 20.02 nm, and pore volume is 0.0182 cm<sup>3</sup>·g<sup>-1</sup>, indicating that this material is mesoporous. The adsorption-desorption curves of SML were drawn by changing the pressure and using the BJH method in the nitrogen condition, and the appearance of the hysteresis loop at 0.65 P/P<sub>0</sub> reveals that the magnetic adsorbent has slit-like holes formed by a loose polymer. Additionally, in Fig. 6(b), the curve belongs to the H<sub>3</sub> hysteresis loop(Liu et al. 2005), and this conclusion is consistent with the material properties of SA polymer. The absence of adsorption limitation in the relatively high-pressure region indicates that the present material is a mesoporous material with a relatively superior adsorption performance.

XPS analysis

Figure 7 shows the elements change on SML before and after the adsorption of Zn (II). As revealed in Figure 7(a), the Zn2p peak appeared, and the strength of Ca2s peak weakens after adsorption, indicating an ion exchange in the adsorption system of the Ca and Zn. The change in N1s peak is shown in Figure 7(b). The binding energy of amino shifted from 400.13 to 399.18 eV, which shows that the nitrogen-containing groups in L-met were involved in the reaction. The spectrum of O1s is presented in Figure 7(c). A shift in the binding energy of C=O-O, C-O, and C=O shifted from 533.9 eV, 532.9 eV, and 531.7 eV to 534.06 eV, 532.77eV, and 531.55 eV, respectively, which indicated that the binding energy of oxygen-

containing groups has changed after adsorption. We conclude that oxygen-containing groups coordinated with Zn(II) (Sun et al. 2019). Additionally, FTIR analysis results showed the presence of carboxyl and amino groups, confirming that these two groups are participating in the adsorption process of heavy metal ions. The Zn2p spectrum in Figure 7(d) is composed of two peaks, representing the formation of Zn-O and Zn-N. According to the Lewis acids and bases and hard-soft-acid-base theory, the existence of electron-donating groups is the reason for the adsorption of the material and the divalent metal ion. The transfer of O and N lone pairs of electrons during the adsorption process causes changes in binding energy, indicating that the donor atoms (O and N) have a coordination effect with Zn(II) (Matlock et al. 2002). Additionally, the adsorption process is affected by the ion exchange effect of Ca(II).

### Concentration analysis of Ca(II) after adsorption of SML on Zn(II)

The concentration of Ca(II), shown in Fig. 8, is after the adsorption of SML on Zn(II). The sorption ability of SML for Zn(II) was  $1.128 \text{ mmol}\cdot\text{g}^{-1}$ , and the release of Ca(II) in the adsorbent was  $0.6258 \text{ mmol}$  at a concentration of  $100 \text{ mg}\cdot\text{L}^{-1}$ . At this concentration, the capacity of adsorption and release of Ca(II) in SML tended to balance, and the contribution of ion exchange in adsorption was approximately 48.98%. We conclude that the Ca(II) in the gel spheres underwent ion exchange with heavy metal and separated into solution, whereas the Ca(II) used to cross-link was unable to react with heavy metals.

## Conclusion

In this study, a magnetic composite adsorbent is prepared. The adsorption capacity and magnetic reaction properties were combined to the maximum. Experimental results showed that the adsorbent adsorbed up to  $86.86 \text{ mg}\cdot\text{L}^{-1}$  of Zn(II) under optimal conditions. SEM and VSM analysis results indicated that the adsorbent had outstanding magnetic response properties. After five cycles of performance test experiments, the adsorption ability of SML can still be maintained at more than 65% of the largest adsorption amount, and the loss of iron is extremely low, making it difficult to cause secondary pollution. The adsorption data were well fitted to the pseudo-second-order equation and the Langmuir equation, respectively, indicating that the adsorption process is mainly controlled by chemisorption, and thermodynamic studies have found that the reaction process is an entropy-increasing heat absorption process. XPS analysis revealed the presence of the ion exchange of heavy metals with Ca(II) and ligands of carboxyl and amino groups with metals in the adsorption process, with ion exchange accounting for 48.98% of Zn(II) adsorption. Thus, we conclude that the adsorbent is practical and has promise because of its adsorption performance and environmental protection aspects.

## Declarations

**Funding information** This research was sponsored by the Guangzhou Key Project of Applied Basic Research (201904020021), GDAS' Project of Science and Technology Development(20210103058).

**Authors' contribution** YS and BBQ conducted experiments and analyzed the data. SWF provided guidance and revisions. LMD provided assistance.

**Data availability** Not applicable.

**Compliance with ethical standards**

**Competing interests** The authors declare that they have no conflict of interest.

**Ethics approval and consent to participate** Not applicable.

**Consent for publication** Not applicable.

## References

1. Chai WS, Cheun JY, Kumar PS, Mubashir M, Majeed Z, Banat F, Ho SH, Show PL (2021) A review on conventional and novel materials towards heavy metal adsorption in wastewater treatment application. *J Clean Prod* 296:126589. <https://doi.org/10.1016/j.jclepro.2021.126589>
2. Deghles A, Hamed O, Azar M, Abu Lail B, Azzaoui K, Abu Obied A, Jodeh S (2019) Cellulose with Bidentate Chelating Functionality: An Adsorbent for Metal Ions from Wastewater. *BioResources* 14:6247–6266. <https://doi.org/10.15376/biores.14.3.6247-6266>
3. Fang L, Li L, Qu Z, Xu HM, Xu JF, Yan NQ (2018) A novel method for the sequential removal and separation of multiple heavy metals from wastewater. *J Hazard Mater* 342:617–624. <https://doi.org/10.1016/j.jhazmat.2017.08.072>
4. Fu FL, Wang Q (2011) Removal of heavy metal ions from wastewaters: A review. *J Environ Manage* 92:407–418. <https://doi.org/10.1016/j.jenvman.2010.11.011>
5. Fu YF, Xiao QG, Gao YY, Ning PG, Xu HB, Zhang Y (2018) Direct extraction of Mo(VI) from acidic leach solution of molybdenite ore by ion exchange resin: Batch and column adsorption studies. *T Nonferrous Metal Soc* 28:1660–1669. [https://doi.org/10.1016/s1003-6326\(18\)64809-5](https://doi.org/10.1016/s1003-6326(18)64809-5)
6. Garg A, Mainrai M, Bulasara VK, Barman S (2015) Experimental Investigation on Adsorption of Amido Black 10B Dye onto Zeolite Synthesized from Fly Ash. *Chem Eng Commun* 202:123–130. <https://doi.org/10.1080/00986445.2013.836636>
7. Ghiggi FF, Pollo LD, Cardozo NSM, Tessaro IC (2017) Preparation and characterization of polyethersulfone/N-phthaloyl-chitosan ultrafiltration membrane with antifouling property. *Eur Polym J* 92:61–70. <https://doi.org/10.1016/j.eurpolymj.2017.04.030>
8. Giles NM, Watts AB, Giles GI, Fry FH, Littlechild JA, Jacob C (2003) Metal and redox modulation of cysteine protein function. *Chem Biol* 10:677–693. [https://doi.org/10.1016/s1074-5521\(03\)00174-1](https://doi.org/10.1016/s1074-5521(03)00174-1)
9. Godiya CB, Liang M, Sayed SM, Li DW, Lu XL (2019) Novel alginate/polyethyleneimine hydrogel adsorbent for cascaded removal and utilization of Cu<sup>2+</sup> and Pb<sup>2+</sup> ions. *J Environ Manage* 232:829–841. <https://doi.org/10.1016/j.jenvman.2018.11.131>

10. Gopalakrishnan Y, Al-Gheethi A, Malek MA, Azlan MM, Al-Sahari M, Mohamed R, Alkhadher S, Noman E (2020) Removal of Basic Brown 16 from Aqueous Solution Using Durian Shell Adsorbent, Optimisation and Techno-Economic Analysis. *Sustainability* 12.  
<https://doi.org/10.3390/su12218928>
11. Gurgel LVA, Gil LF (2009) Adsorption of Cu(II), Cd(II) and Pb(II) from aqueous single metal solutions by succinylated twice-mercerized sugarcane bagasse functionalized with triethylenetetramine. *Water Res* 43:4479–4488. <https://doi.org/10.1016/j.watres.2009.07.017>
12. He GH, Wang C, Cao JL, Fan LH, Zhao S, Chai Y (2019) Carboxymethyl chitosan-kaolinite composite hydrogel for efficient copper ions trapping. *J Environ Chem Eng* 7.  
<https://doi.org/10.1016/j.jece.2019.102953>
13. Hongyu W, Bin G, Shenseng W, June F, Yingwen X, Kai Y (2015) Removal of Pb(II), Cu(II), and Cd(II) from aqueous solutions by biochar derived from KMnO<sub>4</sub> treated hickory wood. *Bioresource Technol* 197:356–362. <https://doi.org/10.1016/j.biortech.2015.08.132>
14. Hoseinian FS, Irannajad M, Safari M (2017) Effective factors and kinetics study of zinc ion removal from synthetic wastewater by ion flotation. *Sep Sci Technol* 52:892–902.  
<https://doi.org/10.1080/01496395.2016.1267216>
15. Huang ZJ, Huang ZY, Feng LJ, Luo XW, Wu PX, Cui LH, Mao XY (2018) Modified cellulose by polyethyleneimine and ethylenediamine with induced Cu(II) and Pb(II) adsorption potentialities. *Carbohydr Polym* 202:470–478. <https://doi.org/10.1016/j.carbpol.2018.08.136>
16. Jiang HM, Yang T, Wang YH, Lian HZ, Hu X (2013) Magnetic solid-phase extraction combined with graphite furnace atomic absorption spectrometry for speciation of Cr(III) and Cr(VI) in environmental waters. *Talanta* 116:361–367. <https://doi.org/10.1016/j.talanta.2013.05.008>
17. Jin QH, Cui CY, Chen HY, Wu J, Hu J, Xing X, Geng JF, Wu YH (2019) Effective removal of Cd<sup>2+</sup> and Pb<sup>2+</sup> pollutants from wastewater by dielectrophoresis-assisted adsorption. *Front Env Sci Eng* 13.  
<https://doi.org/10.1007/s11783-019-1092-9>
18. Kumar R, Kumar M, Ahmad R, Barakat MA (2013) L-Methionine modified Dowex-50 ion-exchanger of reduced size for the separation and removal of Cu(II) and Ni(II) from aqueous solution. *Chem Eng J* 218:32–38. <https://doi.org/10.1016/j.cej.2012.12.029>
19. Lin HX, Long JL, Gu Q, Zhang WX, Ruan RS, Li ZH, Wang XX (2012) In situ IR study of surface hydroxyl species of dehydrated TiO<sub>2</sub>: towards understanding pivotal surface processes of TiO<sub>2</sub> photocatalytic oxidation of toluene. *Phys Chem Chem Phys* 14:9468–9474.  
<https://doi.org/10.1039/c2cp40893g>
20. Liu HY, Wang KP, Teng H (2005) A simplified preparation of mesoporous carbon and the examination of the carbon accessibility for electric double layer formation. *Carbon* 43:559–566
21. Liu JX, Wang SQ, Fu JY, Ding XQ, Zhao J (2020) Zn<sup>2+</sup> adsorption from wastewater using a chitosan/beta-cyclodextrin-based composite membrane. *J Food Biochem* 44.  
<https://doi.org/10.1111/jfbc.13483>

22. Mao ML, Yan TT, Shen JJ, Zhang JP, Zhang DS (2021) Capacitive Removal of Heavy Metal Ions from Wastewater via an Electro-Adsorption and Electro-Reaction Coupling Process. *Environ Sci Technol* 55:3333–3340. <https://doi.org/10.1021/acs.est.0c07849>
23. Matlock MM, Howerton BS, Atwood DA (2002) Chemical precipitation of heavy metals from acid mine drainage. *Water Res* 36:4757–4764. [https://doi.org/10.1016/S0043-1354\(02\)00149-5](https://doi.org/10.1016/S0043-1354(02)00149-5)
24. Mousa NE, Simonescu CM, Patescu RE, Onose C, Tardei C, Culita DC, Oprea O, Patroi D, Lavric V (2016) Pb<sup>2+</sup> removal from aqueous synthetic solutions by calcium alginate and chitosan coated calcium alginate. *React Funct Polym* 109:137–150. <https://doi.org/10.1016/j.reactfunctpolym.2016.11.001>
25. Skubiszewska-Zieba J, Charmas B, Koltowski M, Oleszczuk P (2017) Active carbons from waste biochars Structural and thermal properties. *J Therm Anal calorim* 130:15–24. <https://doi.org/10.1007/s10973-017-6143-5>
26. Soltani H, Belmokhtar A, Zeggai FZ, Benyoucef A, Bousalem S, Bachari K (2019) Copper(II) Removal from Aqueous Solutions by PANI-Clay Hybrid Material: Fabrication, Characterization, Adsorption and Kinetics Study. *J Inorg Organomet P* 29:841–850. <https://doi.org/10.1007/s10904-018-01058-z>
27. Song T, Yu C, He X, Lin J, Liu ZY, Yang XJ, Zhang YJ, Huang Y, Tang CC (2018) Synthesis of magnetically separable porous BN microrods@Fe<sub>3</sub>O<sub>4</sub> nanocomposites for Pb(II) adsorption. *Colloid Surface A* 537:508–515. <https://doi.org/10.1016/j.colsurfa.2017.10.060>
28. Sun JT, Li MF, Zhang ZH, Guo JJ (2019) Unravelling the adsorption disparity mechanism of heavy-metal ions on the biomass-derived hierarchically porous carbon. *Appl Surf Sci* 471:615–620. <https://doi.org/10.1016/j.apsusc.2018.12.050>
29. Thasneema KK, Dipin T, Thayyil MS, Sahu PK, Messali M, Rosalin T, Elyas KK, Saharuba PM, Anjitha T, Ben Hadda T (2021) Removal of toxic heavy metals, phenolic compounds and textile dyes from industrial waste water using phosphonium based ionic liquids. *J Mol Liq* 323. <https://doi.org/10.1016/j.molliq.2020.114645>
30. Varghese AG, Paul SA, Latha MS (2019) Remediation of heavy metals and dyes from wastewater using cellulose-based adsorbents. *Environ Chem Lett* 17:867–877. <https://doi.org/10.1007/s10311-018-00843-z>
31. Wang F, Lu XW, Li XY (2016) Selective removals of heavy metals (Pb<sup>2+</sup>, Cu<sup>2+</sup>, and Cd<sup>2+</sup>) from wastewater by gelation with alginate for effective metal recovery. *J Hazard Mater* 308:75–83. <https://doi.org/10.1016/j.jhazmat.2016.01.021>
32. Wang LL, Li H, Yu DY, Wang YJ, Wang W, Wu M (2019) Hyperbranched polyamide-functionalized sodium alginate microsphere as a novel adsorbent for the removal of antimony(III) in wastewater. *Environ Sci Pollut R* 26:27372–27384. <https://doi.org/10.1007/s11356-019-05914-4>
33. Yahaya YA, Don MM, Bhatia S (2009) Biosorption of copper (II) onto immobilized cells of *Pycnoporus sanguineus* from aqueous solution: Equilibrium and kinetic studies. *J Hazard Mater* 161:189–195

34. Yavuz CT, Mayo JT, Yu WW, Prakash A, Falkner JC, Yean S, Cong LL, Shipley HJ, Kan A, Tomson M, Natelson D, Colvin VL (2006) Low-field magnetic separation of monodisperse Fe<sub>3</sub>O<sub>4</sub> nanocrystals. *Science* 314:964–967. <https://doi.org/10.1126/science.1131475>
35. Zhang N, Zhang HH, Li R, Xing YJ (2020) Preparation and adsorption properties of citrate-crosslinked chitosan salt microspheres by microwave assisted method. *Int J Biol Macromol* 152:1146–1156. <https://doi.org/10.1016/j.ijbiomac.2019.10.203>
36. Zhang S, Xu F, Wang YF, Zhang WZ, Peng XL, Pepe F (2013) Silica modified calcium alginate-xanthan gum hybrid bead composites for the removal and recovery of Pb(II) from aqueous solution. *Chem Eng J* 234:33–42. <https://doi.org/10.1016/j.cej.2013.08.102>
37. Zhu YH, Hu J, Wang JL (2012) Competitive adsorption of Pb(II), Cu(II) and Zn(II) onto xanthate-modified magnetic chitosan. *J Hazard Mater* 221:155–161. <https://doi.org/10.1016/j.jhazmat.2012.04.026>

## Figures

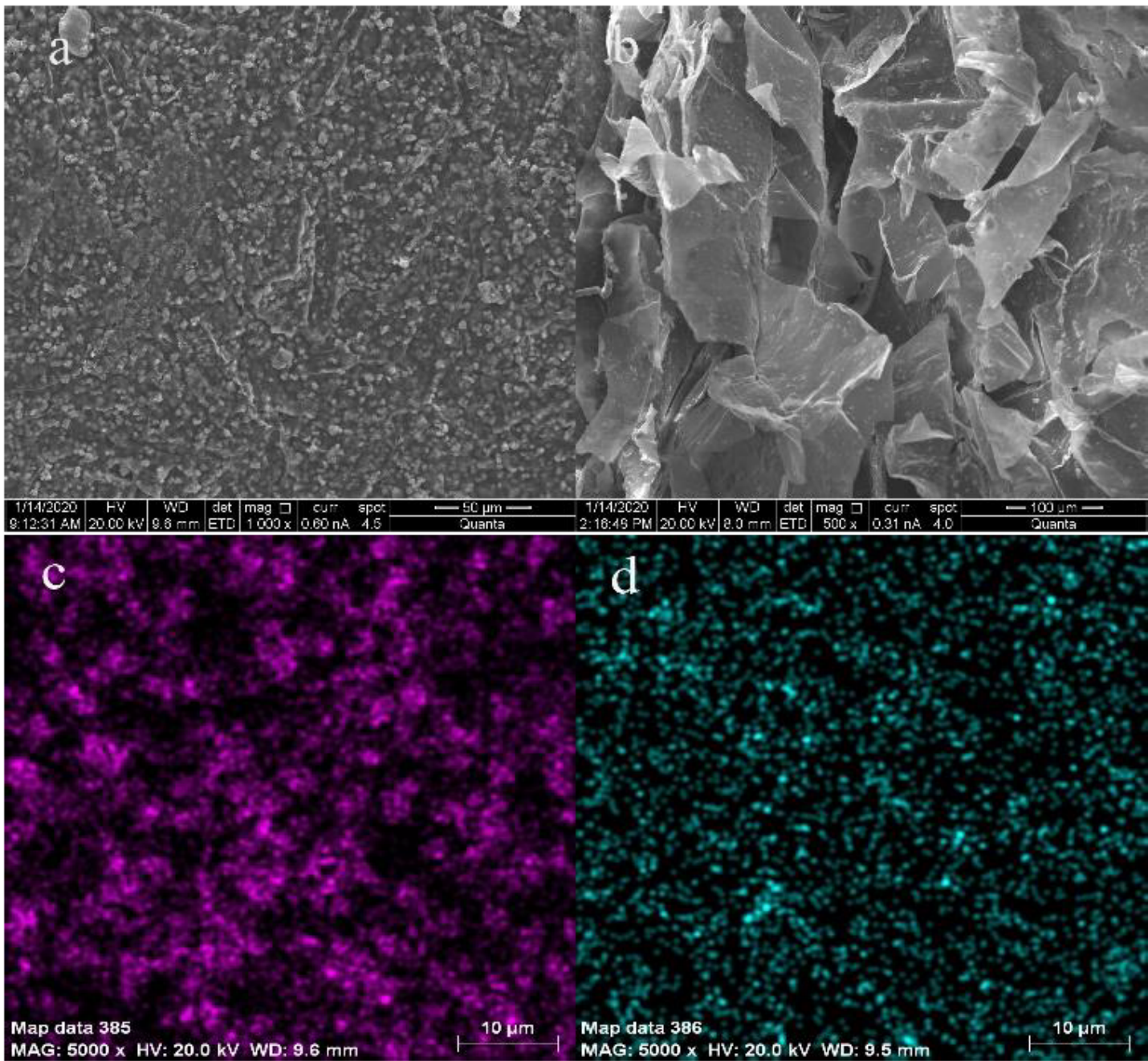


**Figure 1**

SEM images (a) Surface morphology of SML. (b) Cross-sectional view of SML.

(c) Element distribution of Fe. (d) Element distribution of N

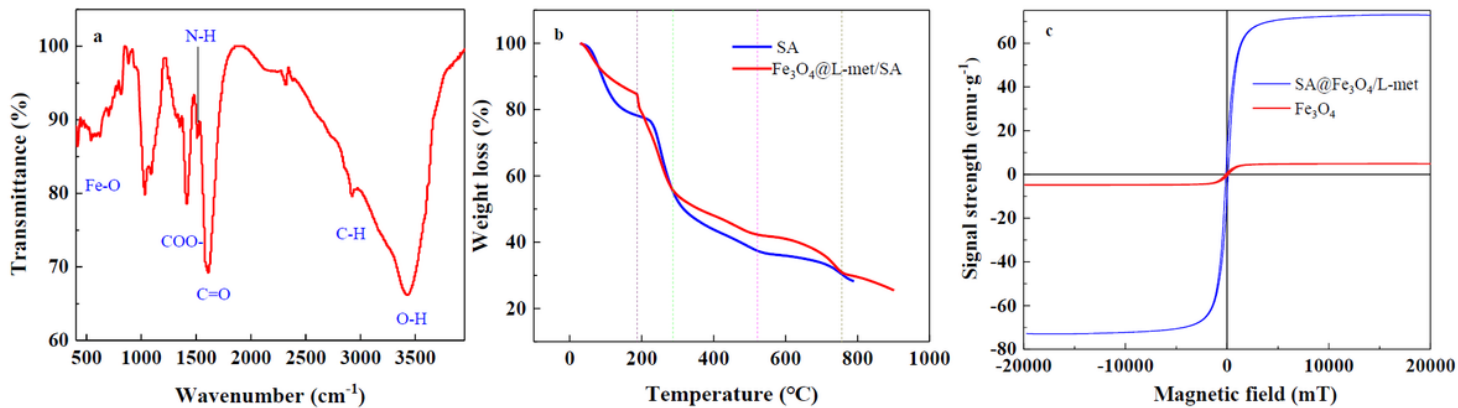


**Figure 2**

(a) Fourier infrared spectrum of SML. (b) Thermogravimetric analysis chart of SML. (c) Hysteresis loop of Fe<sub>3</sub>O<sub>4</sub> and SML

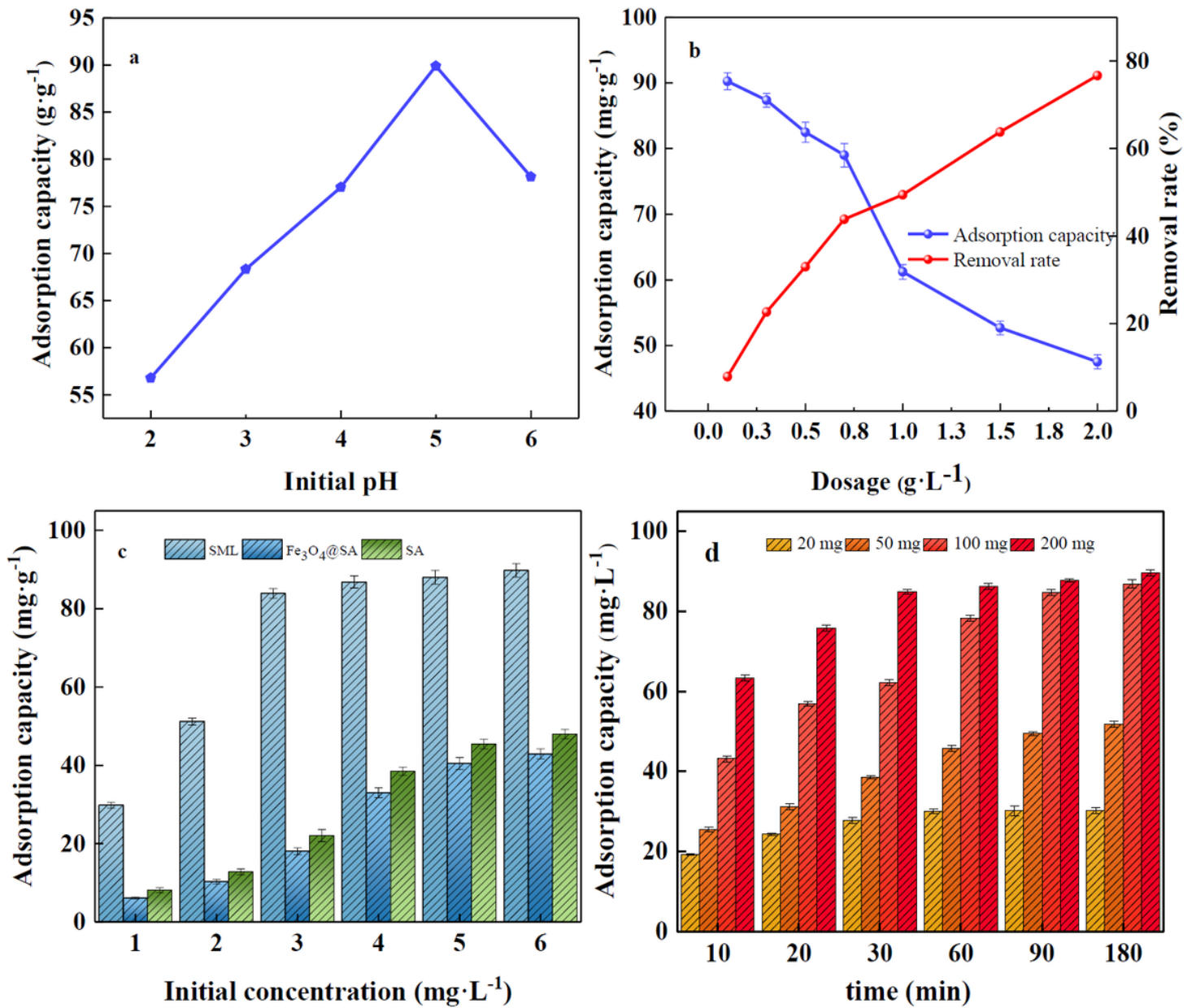


**Figure 3**

(a) Effect of pH on adsorption of Zn(II). (b) Effect of dosage on the adsorption capacity of Zn(II) by SML. (c) Effects of the initial concentration on the adsorption of Zn(II) on different materials. (d) Effect at various starting concentrations of time for Zn(II) adsorption by SML

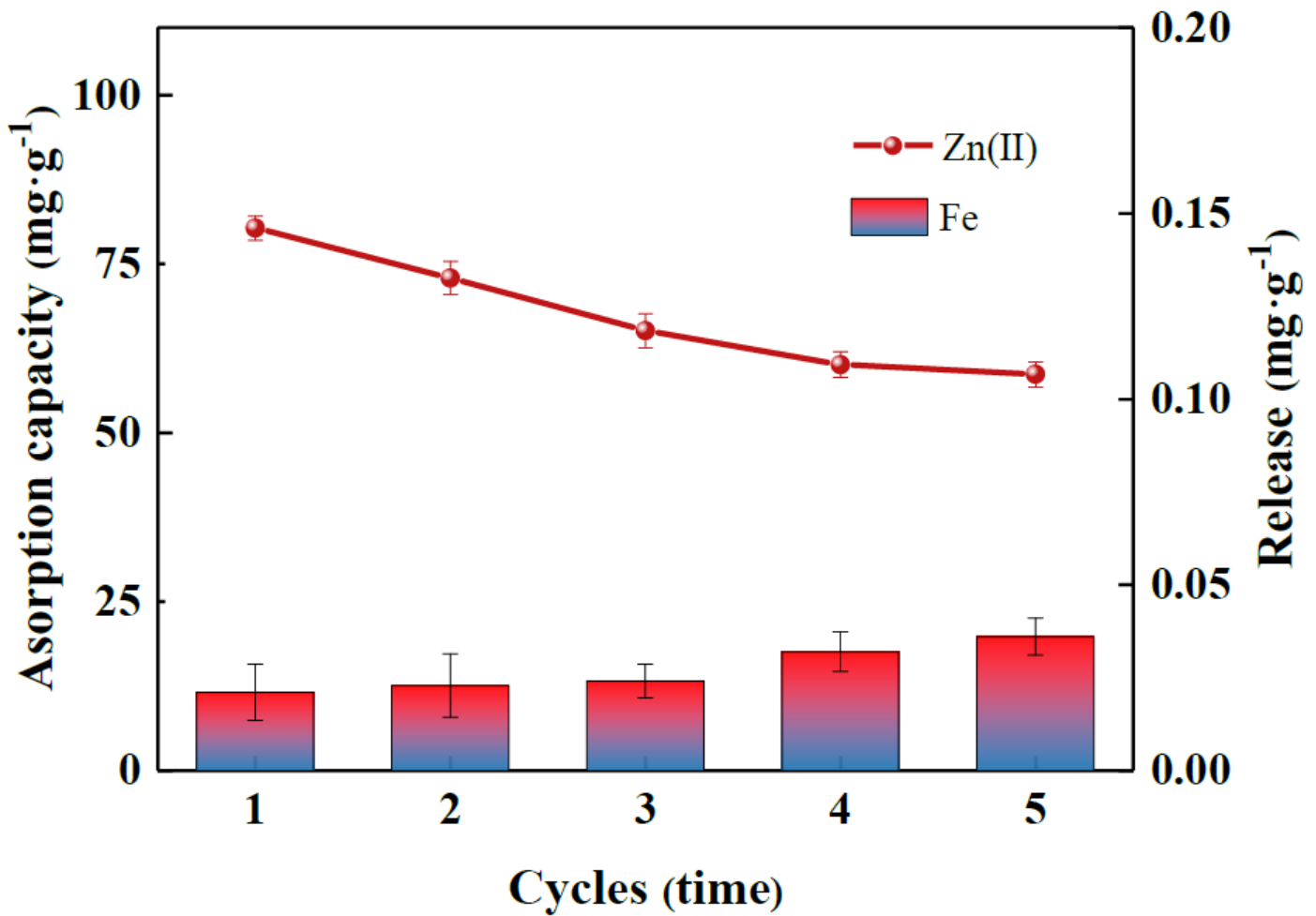


Figure 4

Changes in SML adsorption capacity and Fe loss under the number of cycles

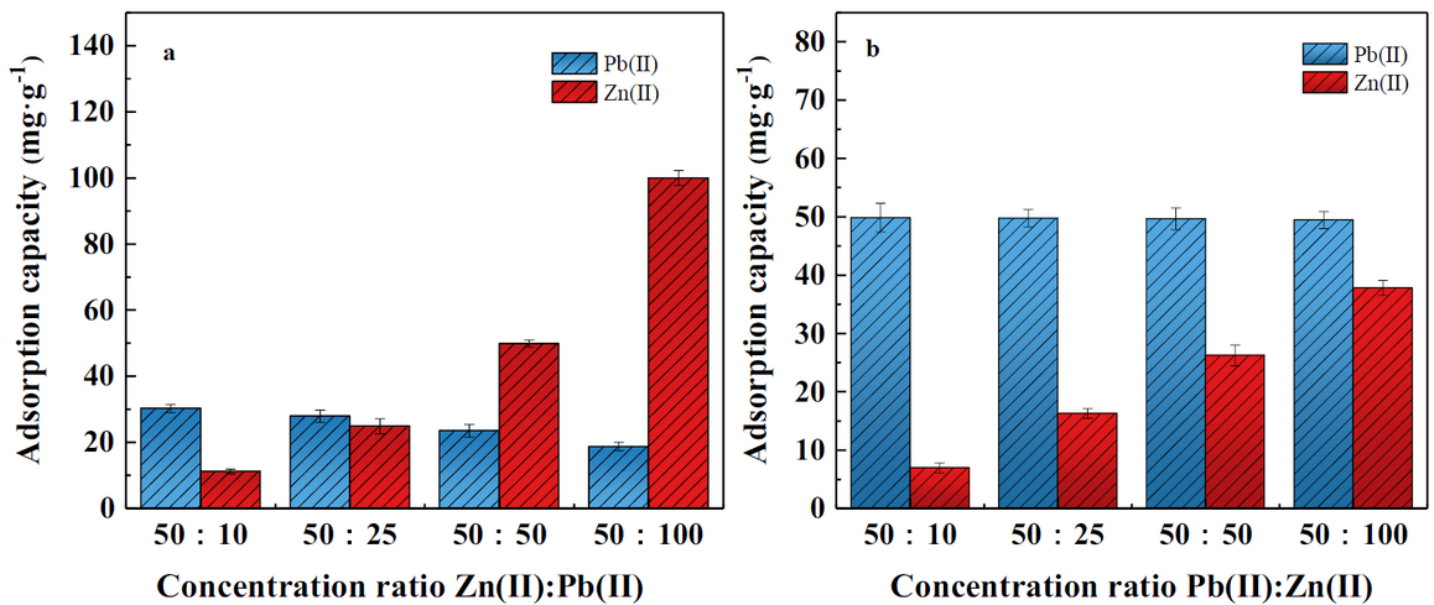


Figure 5

(a) Effect of increasing the quantity of total Pb(II) on Zn(II) sorption by SML (b) Effect of increasing total amount of Zn(II) on sorption of material to Pb(II)

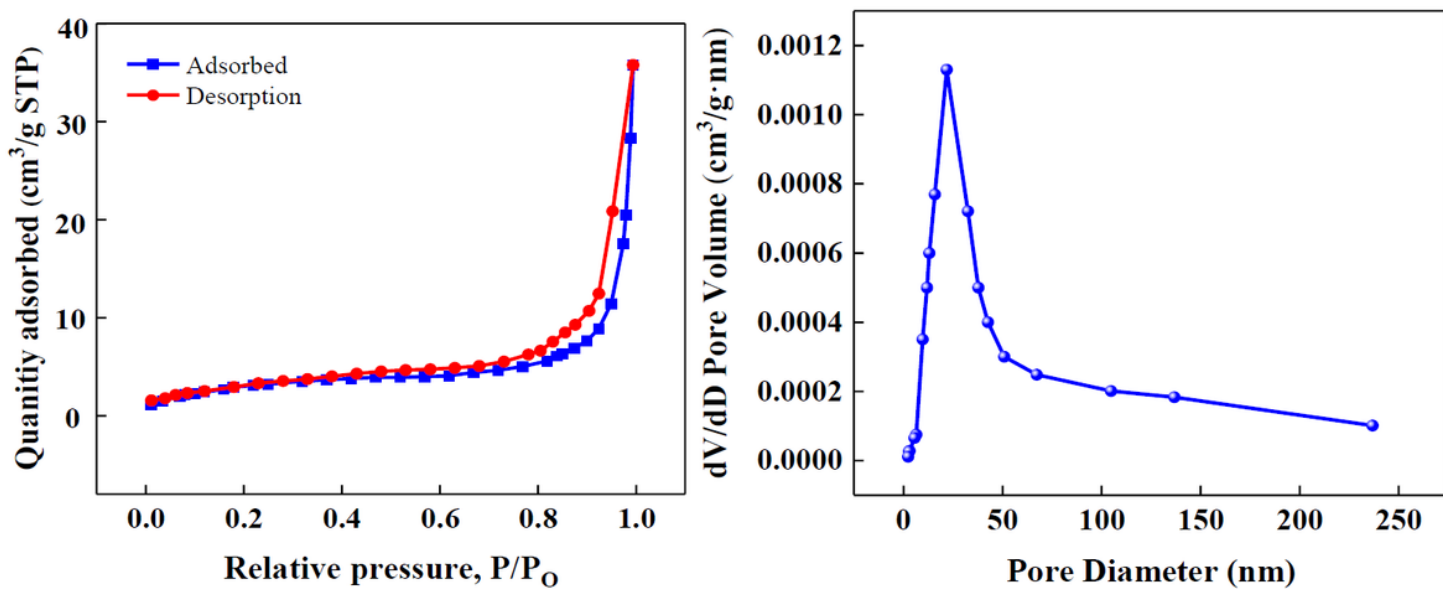
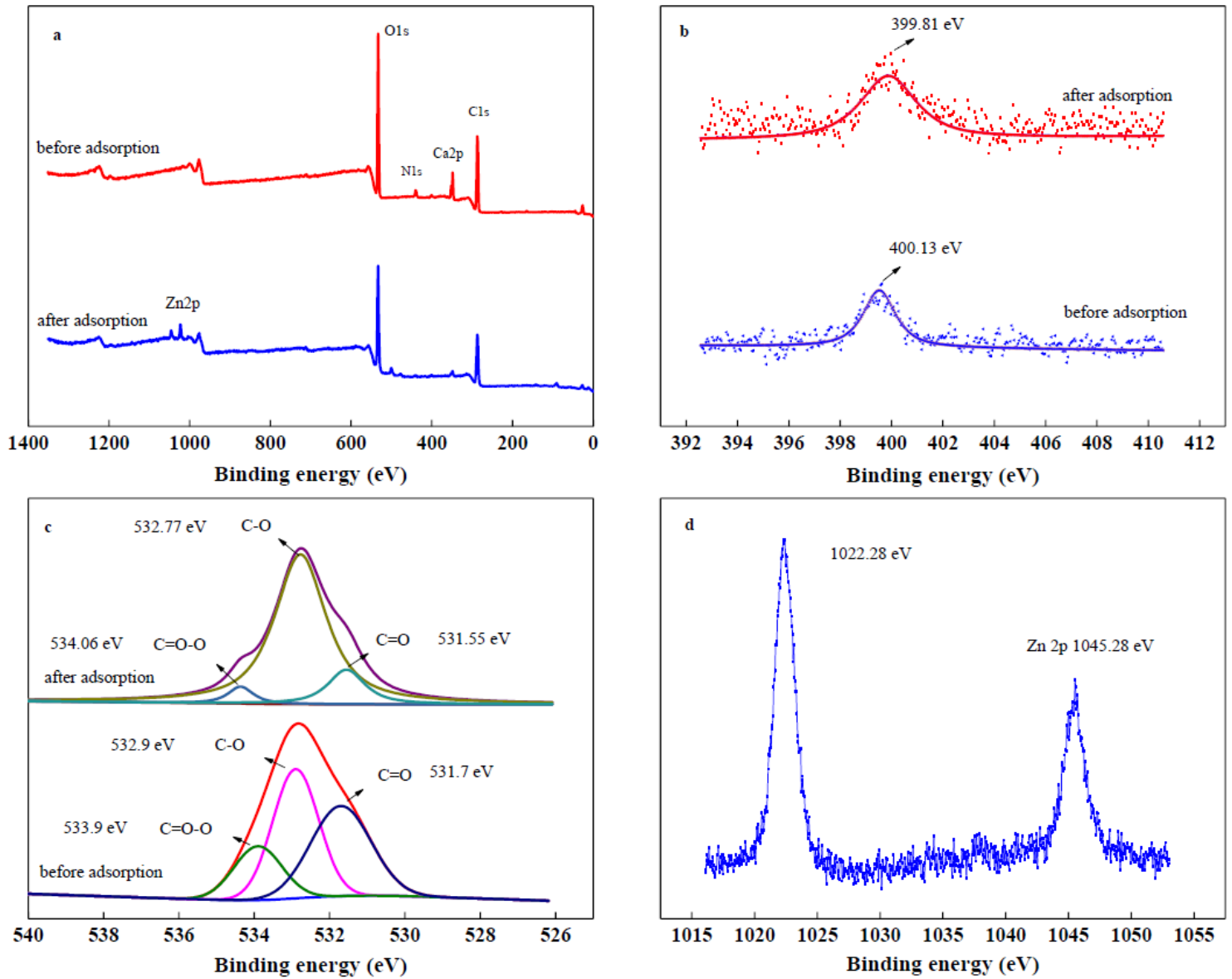


Figure 6

(a) Pore size distribution (b) Adsorption-desorption isotherms



**Figure 7**

(a) XPS full spectrum of Zn adsorption for SML. (b) Narrow spectrum of N pre and post the adsorption of Zn. (c) Narrow spectrum of O pre and post the adsorption of Zn. (d) Narrow spectrum of Zn pre and post the adsorption of Zn

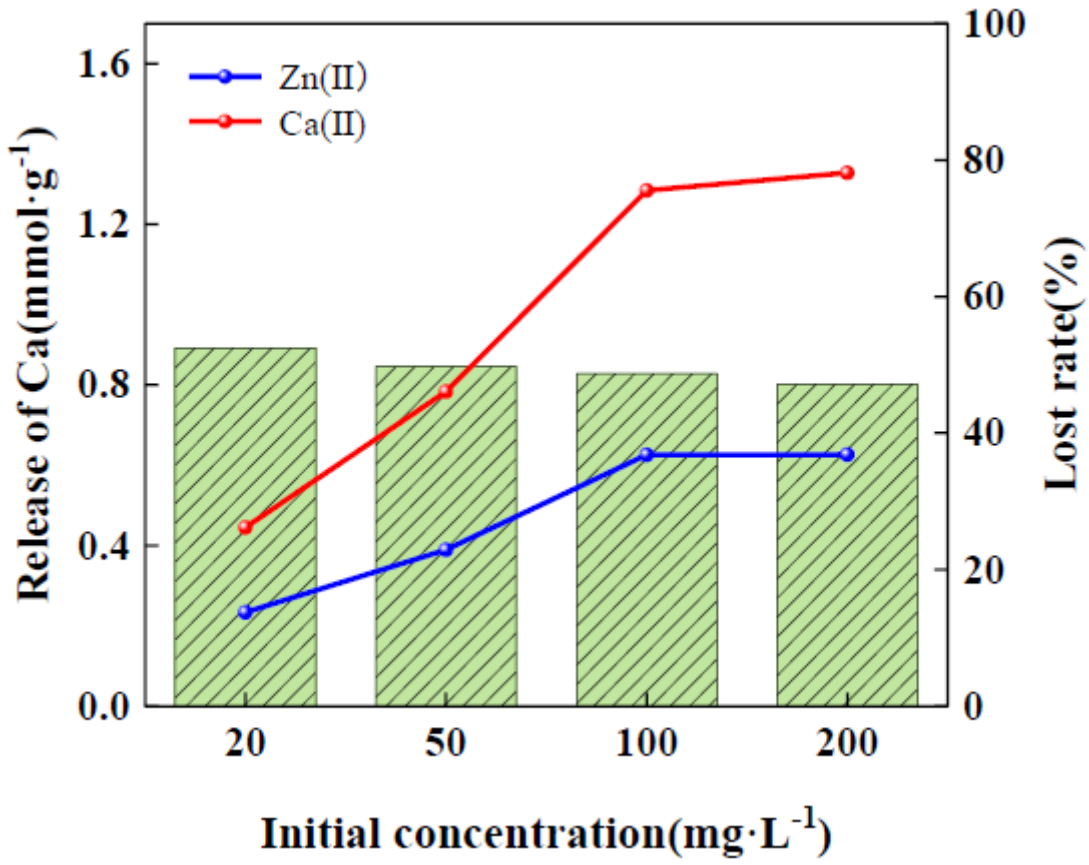


Figure 8

Ca(II) concentration after adsorption of SML